Mechanics & Industry **24**, 3 (2023)

https://doi.org/10.1051/meca/2022029

Mechanics & Industry

Available online at:
www.mechanics-industry.org

REGULAR ARTICLE

OPEN ACCESS

Study on elastohydrodynamic lubrication performance of double-layer composite water-lubricated bearings

Zhen Yang[1,2], Xiuli Zhang[1,2,*], Yanzhen Wang[3] and Yuanliang Zhao[1,2]

[1] School of Mechanical Engineering, Shandong University of Technology, Zibo, China
[2] Shandong Provincial Key Laboratory of Precision Manufacturing and Non-traditional Machining, Shandong University of Technology, Zibo, China
[3] Marine Design and Research Institute of China, Shanghai, China

Received: 12 August 2022 / Accepted: 12 December 2022

Abstract. Double-layer composite water-lubricated bearing is a new type of water-lubricated bearing which can integrate the good damping performance of low elastic under-layer bush and good tribological performance of plastic layer bush. This paper analyzes its elastohydrodynamic lubrication performance by fluid–structure interaction (FSI) method, and studies the effects of eccentricity ratio, rotational speed, elastic modulus distribution and thickness distribution of bearing bush on its lubrication performance. Results show that the lubrication performance of double-layer bearing is more like that of plastic bearing. As rotational speed and eccentricity ratio increase, the maximum water film pressure, the load carrying capacity and the maximum bush deformation increase significantly. As the elastic modulus of the low elastic under-layer bush decreases, the total bush deformation increases significantly, but the load carrying capacity decreases slightly. The bush thickness distribution influences the deformation distribution of both low elastic under-layer bush and plastic layer bush, but have little impact on the total bush deformation and bearing lubrication performance.

Keywords: Double-layer bush / water lubrication / journal bearing / elastohydrodynamic lubrication / fluid–structure interaction

1 Introduction

Water-lubricated bearings have the characteristics of environmental protection and energy conservation, and are now widely used in ship propulsion system, nuclear main pump, water turbine and other hydraulic machinery. At present, stern tube water-lubricated bearings mainly use rubber as bush material, because rubber has good damping performance and can weaken the adverse effect of journal misalignment and vibration. But rubber bearings have large bush deformation and low hydrodynamic load carrying capacity, and the large friction coefficient usually causes high power consumption and noise [1,2]. In order to improve the bearing load carrying capacity and reduce power consumption, some turbine and marine pump water-lubricated bearings use plastic such as polytetrafluoroethylene (PTFE) and ultra-high molecular weight polyethylene (UHMWPE) as bush material [3–6]. While plastics have low friction coefficient, but worse compliance and damping properties than rubber. In recent years, some research institutions and researchers have studied double-layer composite water-lubricated bearings. Duramax Marine has developed a double-layer stern tube bearing ROMOR I with nitrile rubber (NBR) as one layer bush and UHMWPE as the other, which has been applied in US surface ships and submarines [7]. Litwin [8–10] studied the lubrication performance of a three-layer water-lubricated bearing (bronze-NBR-PTFE). Results show that the bearing works under hydrodynamic lubrication state for most conditions, and its running resistance is less than the NBR bearing.

As a new kind of water-lubricated bearing, the double-layer composite bearing has not been studied extensively. But many scholars have studied the lubrication characteristics of water-lubricating rubber bearings or plastic bearings. Cabrera et al. [11] studied the film pressure distribution in water-lubricated rubber journal bearings by experiments, and found that the bearings operate in the regime of mixed lubrication. Due to the elastic deformation of rubber, the film pressure profiles are obviously different from those of rigid bearings, and peak pressures are greatly reduced. Kraker et al. [12] calculated the Stribeck curves for water-lubricated journal bearings

* e-mail: zhangxiulli@163.com

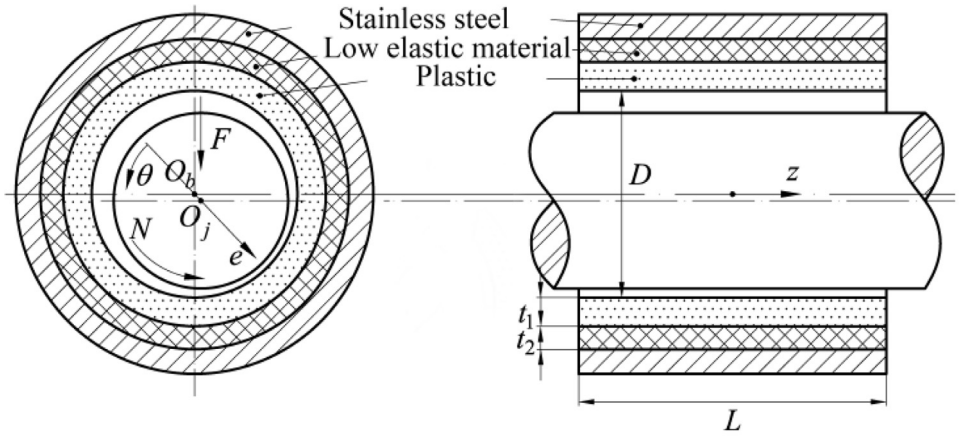

Fig. 1. Water-lubricated double-layer bearing.

by a mixed elastohydrodynamic lubrication model, and found that within a certain range, the smaller the radial clearance, surface roughness, external load and elastic modulus of the bearing, the smaller the rotational speed at the mixed lubrication (ML) to elastohydrodynamic lubrication (EHL) transition. Liao et al. [13] studied the effects of different lubricants (pure water, saline and sandy water) on the lubricating properties of water-lubricated rubber bearings. Results showed that the water film pressure of the bearing generally increases and stabilizes with increasing rotational speed and eccentricity, but sandy water shows a greater increase compared with saline and pure water. The deformation and the stress of the carrying surface shows the same trend. Wang et al. [14] studied the lubrication characteristics of water-lubricated bearing by CFD and FSI method. Results showed that the bearing bush deformation reduces the water film pressure and increases the film thickness, which reduces the bush stress concentration. Lao et al. [15] modified UHMWPE by adding Polyimide (PI) and studied its tribological performance in artificial seawater. They found that the modified material has the lowest friction coefficient and wear height than Thordon, Tenmat, and PEEK. Zhou et al. [16,17] studied the friction coefficient, water film pressure and shaft orbits of multiple groove rubber alloy bearing, and compared the Stribeck curve of straight groove and spiral groove bearing. Results showed that groove and bearing bush deformation have a great influence on the pressure distribution of bearing, and spiral groove bearing has better lubrication performance than straight groove bearing. Zhao and Rui [18] studied the hydrodynamic characteristics of a water-lubricated rubber journal bearing with a large aspect ratio by finite difference numerical method and experiments. They found that the liquid film was not continuous at low speeds. Wang et al. [19] studied the tribological properties of the rubber bearings under different loads and velocities. The experimental results showed that the friction coefficient decreases with increasing velocity, the friction coefficient increases at first and then decreases with increasing load. Huang et al. [20] studied the dynamic performance of a water-lubrication rubber bearing with rubber damping layer, and found that the damping layer can reduce bearing vibration, especially under high rotational speed and high load conditions. Xiang et al. [21] explored nonlinear dynamic mixed friction behaviors of Thorlon water-lubricated bearings.

Although the double-layer composite water-lubricated bearing has been confirmed to have superior properties, due to the large difference in the elastic modulus of low elastic under-layer bush and plastic layer bush, the bush deformation of this kind of bearing is quite different from those of water-lubricated rubber bearing and plastic bearing, and its lubrication performance is also different. Therefore, this paper built a fluid–structure interaction model of double-layer composite water-lubricated bearing to analyze its elastohydrodynamic lubrication performance, and studied the influence of eccentricity ratio, rotational speed, elastic modulus distribution and thickness distribution of the double-layer bush on the lubrication performance of this kind of bearing, so as to provide reference for the design of such bearings.

2 Bearing structure and parameters

Figure 1 shows the structure of the double-layer composite water-lubricated bearing. The low elastic under-layer bush is between the plastic layer bush and stainless-steel sleeve. There is radial clearance, c, between bearing and journal. Under external load, when the journal rotates, the journal center O_j is away from the bearing center O_b, forming wedge-shaped lubrication film and generating dynamic pressure and load carrying capacity to support the external load. Parameters affecting the bearing load carrying capacity include journal rotational speed N, bearing inner diameter D, bearing length L, plastic bush layer thickness t_1, plastic layer bush elastic modulus E_1 and Poisson's ratio ν_1, low elastic under-layer bush thickness t_2, low elastic under-layer bush elastic modulus E_2 and Poisson's ratio ν_2, radial clearance c, journal eccentricity ratio ε $(=e/c)$, viscosity of lubricant μ, etc. e-θ-z is the coordinate system.

3 Simulation analysis method

3.1 Governing equations

The basic equations for solving the fluid model are mass conservation equation, momentum conservation equation and energy conservation equation. As the temperature rise of water-lubricated bearing is very small, the temperature change is ignored and the energy conservation equation is not considered in the calculation, ⊗ the fluid inside bearings are taken as incompressible.

The mass conservation equation (the continuous equation) is expressed as:

$$\frac{\partial \rho}{\partial t} + \nabla\cdot(\rho \boldsymbol{v}) = 0, \tag{1}$$

where ρ is the fluid density, $\boldsymbol{v}$ is the fluid velocity vector, $\nabla\cdot\boldsymbol{a} = div\boldsymbol{a} = \frac{\partial a_x}{\partial x} + \frac{\partial a_y}{\partial y} + \frac{\partial a_z}{\partial z}$.

The momentum conservation equation (Navier-Stokes equation) is given as:

$$\frac{\partial}{\partial \mathrm{t}}(\rho \boldsymbol{v}) + \nabla\cdot(\rho \boldsymbol{v} \otimes \boldsymbol{v}) = -\nabla \boldsymbol{p} + \nabla\cdot\boldsymbol{\tau} + \rho \boldsymbol{g} + F, \tag{2}$$

where p is the static pressure, $\boldsymbol{\tau}$ is the stress tensor, $\rho \boldsymbol{g}$ and $\boldsymbol{F}$ are the gravitational force and external body force. Stress tensor $\boldsymbol{\tau}$ is defined as:

$$\tau = \mu(\nabla \boldsymbol{v} + \nabla \boldsymbol{v}^T), \tag{3}$$

where μ is the fluid viscosity.

When the pressure is reduced to a certain value, the water will evaporate, so the cavitation model needs to be coupled with the above equations to calculate the pressure distribution. This paper uses the Zwart-Gerber-Belamri cavitation model in ANSYS FLUENT. The mass transfer of liquid and gas (evaporation and condensation) is governed by the vapor transport equation [22]:

$$\frac{\partial}{\partial t}(\alpha_v \rho_v) + \nabla\cdot(\alpha_v \rho_{\boldsymbol{v}} \boldsymbol{v}) = R_g - R_c, \tag{4}$$

where α_v is the vapor volume fraction, ρ_v is the vapor density, R_g and R_c are the mass transfer source terms connected to the growth and collapse of the vapor bubbles. Zwart-Gerber-Belamri cavitation model assumes that all vapor bubbles in the system have the same size, and R_g and R_c are defined as [23]

$$\text{If} \quad p \le p_v, \quad R_g = F_{evap}\frac{3\alpha_{nuc}(1-\alpha_v)\rho_v}{R_b}\sqrt{\frac{2}{3}\frac{p_v - p}{\rho_l}}, \tag{5}$$

$$\text{If} \quad p \ge p_v, \quad R_c = F_{cond}\frac{3\alpha_v \rho_v}{R_b}\sqrt{\frac{2}{3}\frac{p - p_v}{\rho_l}}, \tag{6}$$

where F_{evap} is the evaporation coefficient, F_{cond} is the condensation coefficient, R_b is the vapor bubble radius, α_{nuc} is the nucleation site volume fraction, ρ_l is the liquid density, p_v is the vapor pressure. In this work, $F_{evap} = 50$, $F_{cond} = 0.01$, $R_b = 10^{-6}$ m, $\alpha_{nuc} = 5 \times 10^{-4}$.

The load carrying capacity can be calculated by integrating the pressure over the journal surface as follows:

$$F_e = \int_0^{2\pi}\int_0^L p\cos\theta R d\theta\, dz$$
$$F_\theta = \int_0^{2\pi}\int_0^L p\sin\theta R d\theta\, dz$$

The total load carrying capacity of bearing is defined as:

$$F = \sqrt{{F_e}^2 + {F_\theta}^2}. \tag{7}$$

The attitude angle is

$$\phi = \arctan\left(\frac{F_\theta}{-F_e}\right). \tag{8}$$

The motion of solid domain is governed by Newton's second law, which can be described as:

$$\rho_s \boldsymbol{a}_s = \nabla\cdot\sigma_s + \boldsymbol{f}_s, \tag{9}$$

where ρ_s is the solid density, $\boldsymbol{a}_s$ is the local acceleration vector of the solid domain, $\boldsymbol{\sigma}_s$ is the solid stress tensor, and $\boldsymbol{f}_s$ is the body force vector.

The displacement d, stress τ, heat flow q, temperature T and other variables of the fluid and solid models are equal on the fluid–solid interface. Ignoring the temperature change, the equilibrium equation can be expressed as:

$$\begin{aligned} \boldsymbol{d}_f &= \boldsymbol{d}_s \\ \tau_f \boldsymbol{n}_f &= \tau_s \boldsymbol{n}_s \end{aligned}, \tag{10}$$

where index f refers to fluid, index s refers to solid.

Two-way FSI analyses were carried out in this work. Figure 2 shows the flowchart of calculation process. The fluid control equations and solid control equations are solved in different solvers respectively, and the calculation results of fluid domain and solid domain are exchanged through the fluid–structure coupling interface. In this work, the water film pressure distribution was solved in FLUENT firstly, and then transferred to Transient Structure to solve the bearing bush deformation. Then the bush deformation distribution was transferred to FLUENT to update the film thickness distribution and calculate the water film pressure. The time step size was 0.02 s and the number of time steps was 50. The maximum number of iterations in FLUENT was 20, and that of the coupling interaction was 5. When the calculation is converged or reaches the number of iterations at this time step, it goes to the next time step. The lift forces are monitored and when the forces remain unchanged, the calculation will be terminated to reduce the processing time.

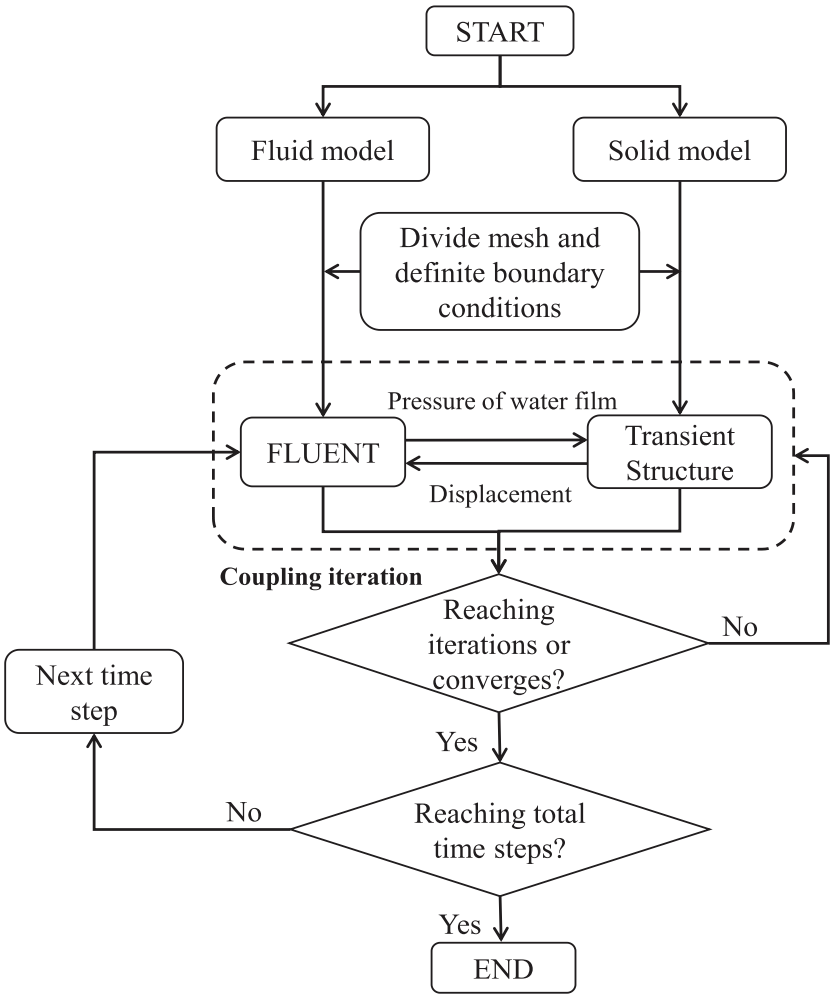

Fig. 2. Flowchart of calculation process.

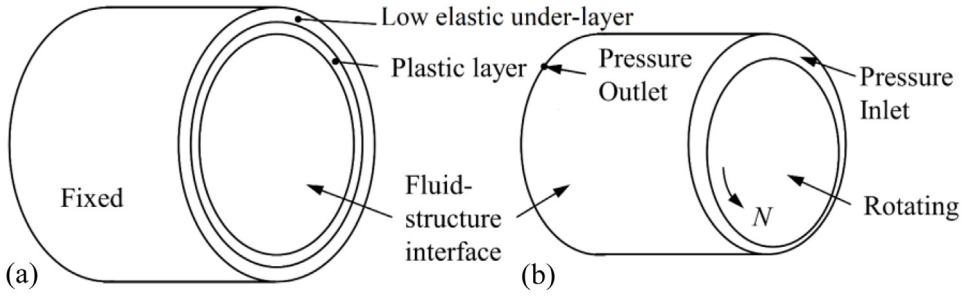

Fig. 3. Model and boundary conditions of (a) Bush and (b) Water film.

3.2 Models

Figure 3a shows the model of composite bush and its boundary condition. The inner surface of the plastic bush is the FSI interface, and the outer surface of the low elastic under-layer bush is fixed. The outer surface of the plastic bush and the inner surface of the low elastic under-layer bush are bonded.

Figure 3b shows the water film model and its boundary condition. In this work the Reynolds number of the fluid is less than 1000, so the viscosity model was set to a laminar model. To consider cavitation, the multiphase flow model was used. The first phase was water liquid, and the second phase was water vapor. The cavitation model is the Zwart-Gerber-Belamari model, and the cavitation pressure is 2340 Pa. The operating pressure is set to 101,325 Pa. Because the bearing is fully submerged, two sides of the water film model are set as "pressure inlet" and "pressure outlet" with gauge pressure as zero Pa. The outer surface of the water film is the FSI interface, and the inner surface is a rotating wall with a rotational speed equal to that of the journal. Figure 4 shows the mesh model of

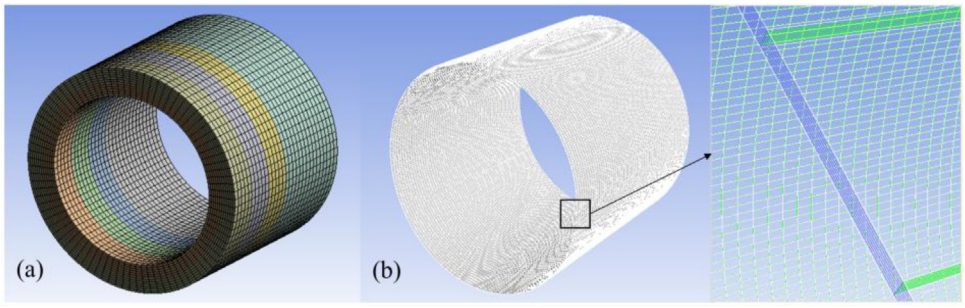

Fig. 4. Mesh model of (a) Bush and (b) Water film.

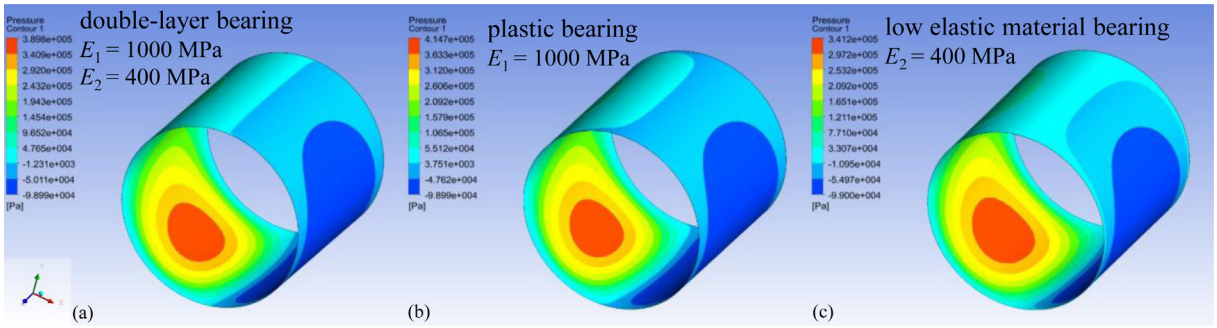

Fig. 5. The water film pressure distribution contour of (a) Double-layer bearing, (b) Plastic bearing, and (c) Low elastic material bearing for $\varepsilon = 0.6$, $N = 1500$ rpm.

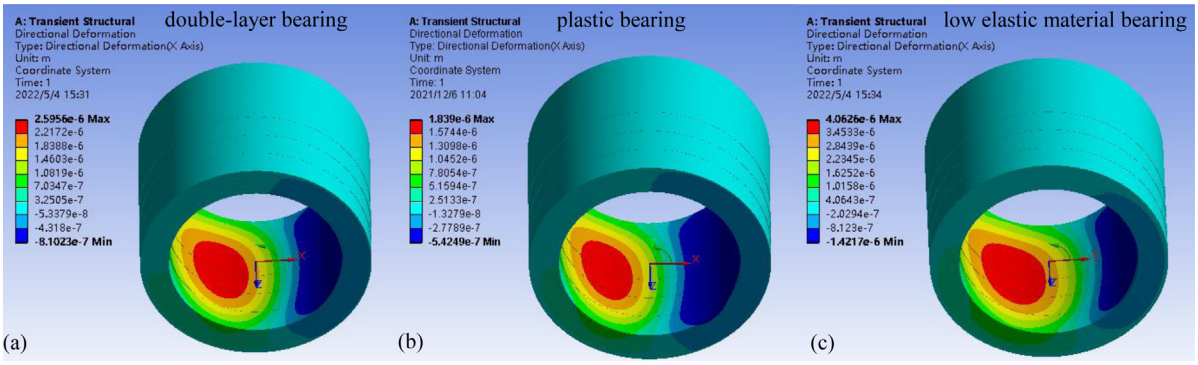

Fig. 6. Bush radial deformation contours of (a) Double-layer bearing, (b) Plastic bearing, and (c) Low elastic material bearing.

bush and water film. All grids are hexahedron grids. The sensitivity of mesh density to results was checked for both the fluid and solid domain. To obtain accurate results, the mesh distributions in the axial, circumferential and radial directions are $60 \times 360 \times 8$ for the water film model, and $60 \times 90 \times 12$ for the bush model.

In the FSI calculation, for models with small bush elastic modulus, negative grids often occur when updating the fluid model mesh, causing calculation error. Thus, in this work the elastic modulus of the low elastic under-layer bush was set as more than 200 MPa. To study the bearings' lubrication performance, the model parameters were set as: $D = 60$ mm, $L/D = 1$, $c = 30\,\mu$m, $E_1 = 1000$ MPa, $E_2 = 200$–1000 MPa, $\nu_1 = 0.4$, $\nu_2 = 0.47$, $t_1 + t_2 = 10$ mm. To compare the lubrication performance of double-layer bearing and those of low elastic material bearing and plastic bearing, the following parameters were used: $\varepsilon = 0.6$, $N = 1500$ rpm, $t_1 = t_2 = 5$ mm, $E_1 = 1000$ MPa, $E_2 = 400$ MPa. To study the influence of eccentricity ratio on the lubrication performance of double-layer bearing, ε ranged from 0.2 to 0.6, and $N = 1500$ rpm, $t_1 = t_2 = 5$ mm, $E_2 = 400$ MPa. To study the influence of the journal rotational speed on the lubrication performance of this kind of bearing, N ranged from 500 rpm to 2500 rpm, and $\varepsilon = 0.6$, $t_1 = t_2 = 5$ mm, $E_2 = 400$ MPa. To study the influence of elastic modulus of low elastic under-layer bush, E_2 ranged from 200 to 1000 MPa, and $\varepsilon = 0.6$, $N = 1500$ rpm, $t_1 = t_2 = 5$ mm. To study the influence of the bearing bush thickness distribution, the low elastic under-layer bush thickness t_2 ranged from 1 to 5 mm, and t_1 ranged from 9 to 5 mm, and $\varepsilon = 0.6$, $N = 1500$ rpm, $E_2 = 400$ MPa.

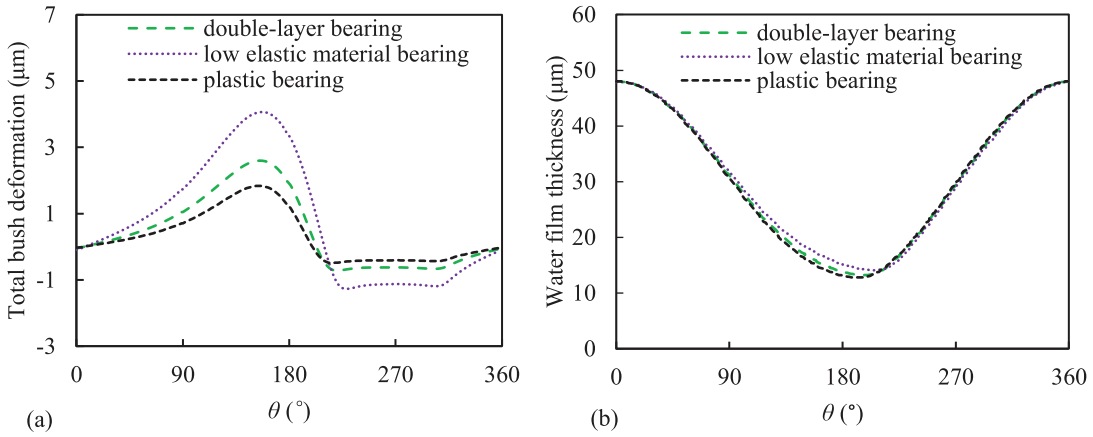

Fig. 7. (a) Bush total deformation distribution, (b) Water film thickness distribution in the mid-plane of bearing.

Table 1. The lubrication performance of the bearings.

Bearing type	p_{max} /MPa	F/N	ϕ/°	f	S/μm
Double-layer bearing ($t_1 = t_2 = 5$ mm)	0.390	835	59.9	0.00272	2.60
Plastic bearing ($t_1 = 10$ mm, $t_2 = 0$)	0.415	854	61.5	0.00269	1.84
Low elastic material bearing ($t_1 = 0$, $t_2 = 10$ mm)	0.340	788	57.3	0.00280	4.06

4 Results and discussion

4.1 Lubrication performance

Figures 5 and 6 compare the water film pressure distribution and the bush radial deformation distribution of double-layer bearing ($t_1 = t_2 = 5$ mm, $E_1 = 1000$ MPa, $E_2 = 400$ MPa, $\nu_1 = 0.4$, $\nu_2 = 0.47$), single-layer plastic bearing ($t_1 = 10$ mm, $t_2 = 0$, $E_1 = 1000$ MPa, $\nu_1 = 0.4$) and single-layer low elastic material bearing ($t_1 = 0$, $t_2 = 10$ mm, $E_2 = 400$ MPa, $\nu_2 = 0.47$) for $\varepsilon = 0.6$, $N = 1500$ rpm. Figure 7 shows the total bush deformation and the water film thickness in the mid-plane of the three kinds of bearings. Table 1 summarizes the lubrication performance parameters of the three kinds of bearings.

It can be seen that the water film pressure contours have positive pressure zone and cavitation zone, and the bush deformation is positive at the positive pressure zone, and negative at the cavitation zone. The maximum bush deformation occurs at the position with the maximum water film pressure. The maximum bush deformation of double-layer bearing, plastic bearing and low elastic material bearing is 2.56 μm, 1.84 μm and 4.06 μm respectively, which means that the maximum bush deformation of double-layer bearing is 0.72 μm more than that of plastic bearing, but 1.5 μm less than that of low elastic material bearing. The minimum water film thickness of low elastic material bearing is larger than those of double-layer bearing and plastic bearing. The maximum water film pressure of double-layer bearing, plastic bearing and low elastic material bearing is 0.39 MPa, 0.415 MPa and 0.34 MPa respectively, and the load carrying capacity is 835 N, 854 N, 788 N respectively. The load carrying capacity of double-layer bearing decreases by 2.22% as compared with that of plastic bearing, but increases by 5.96% as compared with that of low elastic material bearing. The friction coefficient of double-layer bearing, plastic bearing and low elastic material bearing is 0.00272, 0.00269 and 0.00280 respectively, which means that the friction coefficient of double-layer bearing is lower than that of low elastic material bearing and close to plastic bearing. It can be found that the lubrication performance of double-layer bearing is more like that of plastic bearing.

4.2 Effect of eccentricity ratio

Figures 8a–8c shows the radial deformation distribution curves of double-layer bush, low elastic under-layer bush, and plastic layer bush in the mid-plane of bearing for different eccentricity ratio, and $N = 1500$ rpm, $t_1 = t_2 = 5$ mm, $E_1 = 1000$ MPa, $E_2 = 400$ MPa. The plastic layer deformation is equal to the total bush deformation minus the low elastic under-layer deformation. It can be seen that the trend of the deformation curves is similar, and the bush deformation increases significantly as the eccentricity ratio increases. The maximum deformation appears at around $\theta = 153°$. Figure 8d shows the water film thickness distribution for different eccentricity ratio. It can be seen that the minimum water film thickness decreases as the eccentricity ratio rises.

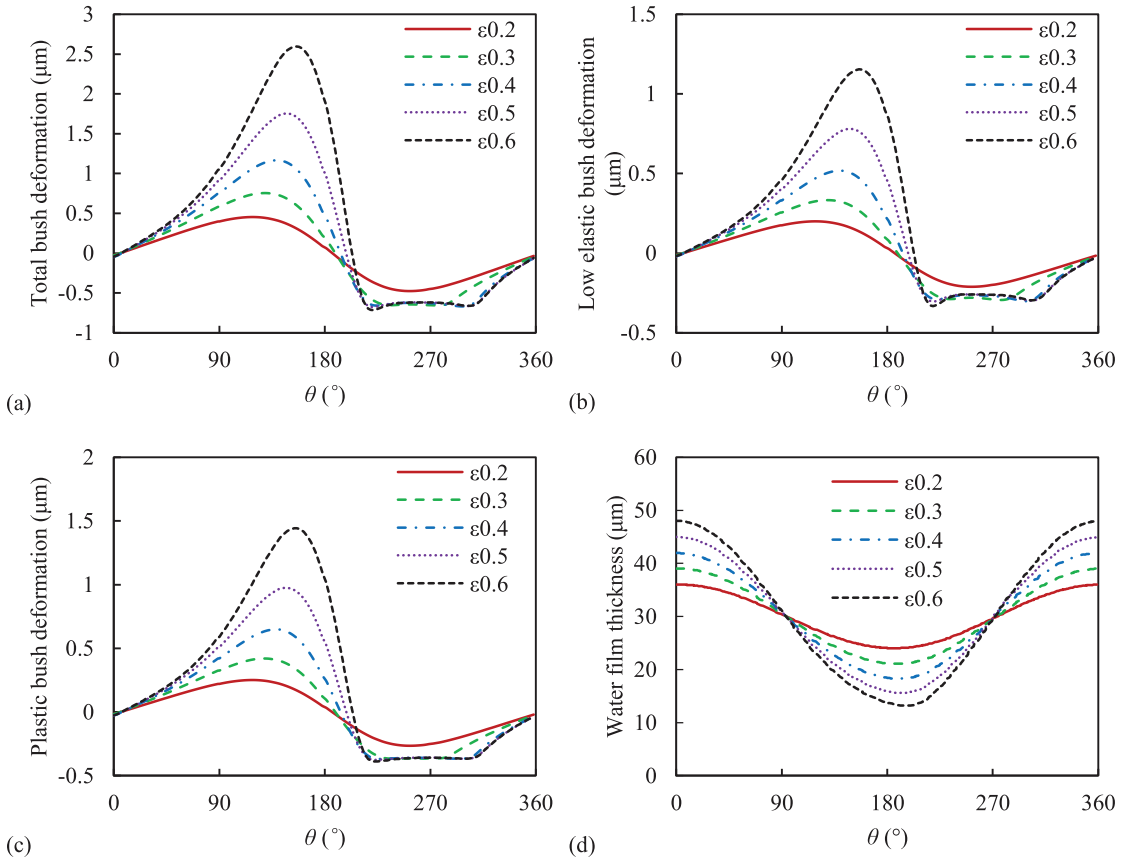

Fig. 8. (a) Bush total deformation distribution, (b) Deformation distribution of low elastic bush, (c) Deformation distribution of plastic layer bush, (d) Water film thickness distribution for different eccentricity ratio ($N = 1500$ rpm, $t_1 = t_2 = 5$ mm, $E_1 = 1000$ MPa, $E_2 = 400$ MPa, $\nu_1 = 0.4$, $\nu_2 = 0.47$).

Figures 9a–9e shows the variation of load carrying capacity, attitude angle, maximum water film pressure, friction coefficient and the maximum bearing bush deformation with eccentricity ratio for different rotational speed. It can be seen that the load carrying capacity, maximum water film pressure and maximum bush deformation increase as the eccentricity ratio rises. The load carrying capacity increases from 431 N to 1255 N as eccentricity ratio moves up from 0.2 to 0.6 for $N = 2500$ rpm. Here it increases about 2.9 times. While without considering the bush deformation, the load carrying capacity increases from 437 N to 1408 N, about 3.2 times. The deformation of bush has a great impact on the lubrication performance of the bearing especially for large eccentricity ratios. For $N = 2500$ rpm, the maximum water film pressure increases from 0.114 MPa to 0.588 MPa, and the maximum deformation of bearing bush increases from 0.75 μm to 3.89 μm. The attitude angle decreases as the eccentricity ratio rises, from 81.9° to 52.6°, and the friction coefficient of the bearing decreases from 0.0071 to 0.0029 as the eccentricity ratio rises.

4.3 Effect of Rotational speed

Figures 10a–10c shows the radial deformation distribution curves of double-layer bush, low elastic under-layer bush, and plastic layer bush in the mid-plane of bearing for different rotational speed. It can be seen that the maximum bush deformation increases significantly as the rotational speed rises. Figure 10d shows the water film thickness for different rotational speed. With the increase of the rotational speed, the water film thickness in the wedge convergence zone increases, and that in the divergent region changes little.

Figures 11a–11e shows the variation of load carrying capacity, attitude angle, maximum water film pressure, friction coefficient and the maximum bearing bush deformation with rotational speed for different eccentricity ratio. It can be seen that the load carrying capacity, maximum water film pressure and maximum bush deformation increase as the rotational speed rises. When without considering the bush deformation, the load carrying capacity and the maximum pressure increase almost linearly with the rotational speed, but after considering the bush deformation, the increasing rate slows down especially for larger rotational speeds. The load carrying capacity increases from 343 N to 1255 N, about 3.7 times, as rotational speed moves up from 500 rpm to 2500 rpm for $\varepsilon = 0.6$. The water film maximum pressure increases from 0.15 MPa to 0.59 MPa, about 3.9 times. The maximum bush deformation increases from 0.98 μm to 3.89 μm. The attitude angle decreases as the rotational speed rises, from 79.8° to 52.6°. The friction coefficient increases from 0.0024 to 0.0029 for $\varepsilon = 0.6$.

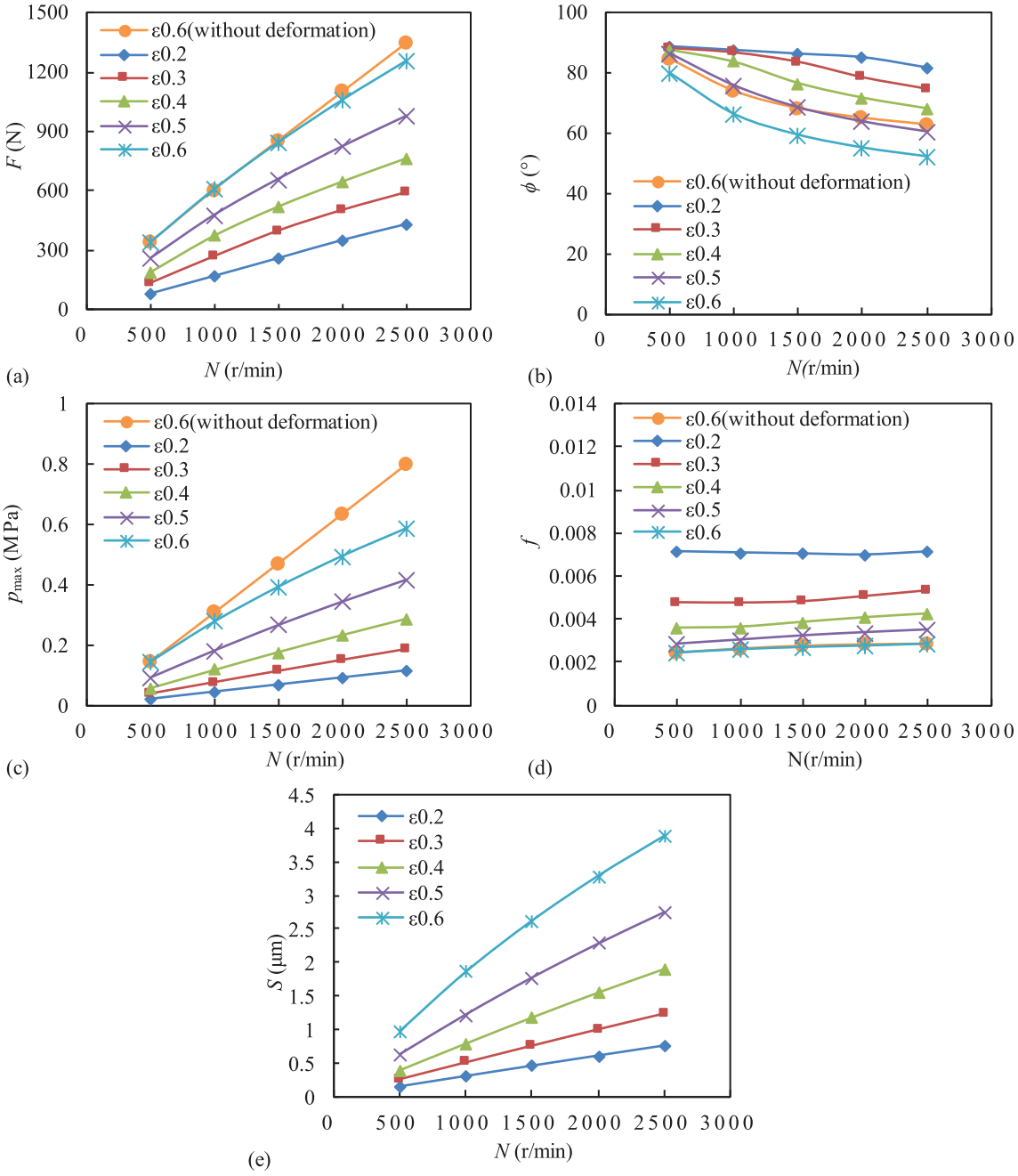

Fig. 9. Effect of eccentricity ratio on the lubrication performance of double-layer bearing (a) Load carrying capacity, (b) Attitude angle, (c) Maximum water film pressure, (d) Friction coefficient, (e) Maximum bearing bush deformation, for t1 = t2 = 5 mm, E1 = 1000 MPa, E2 = 400 MPa, n1= 0.4, n2 = 0.47.

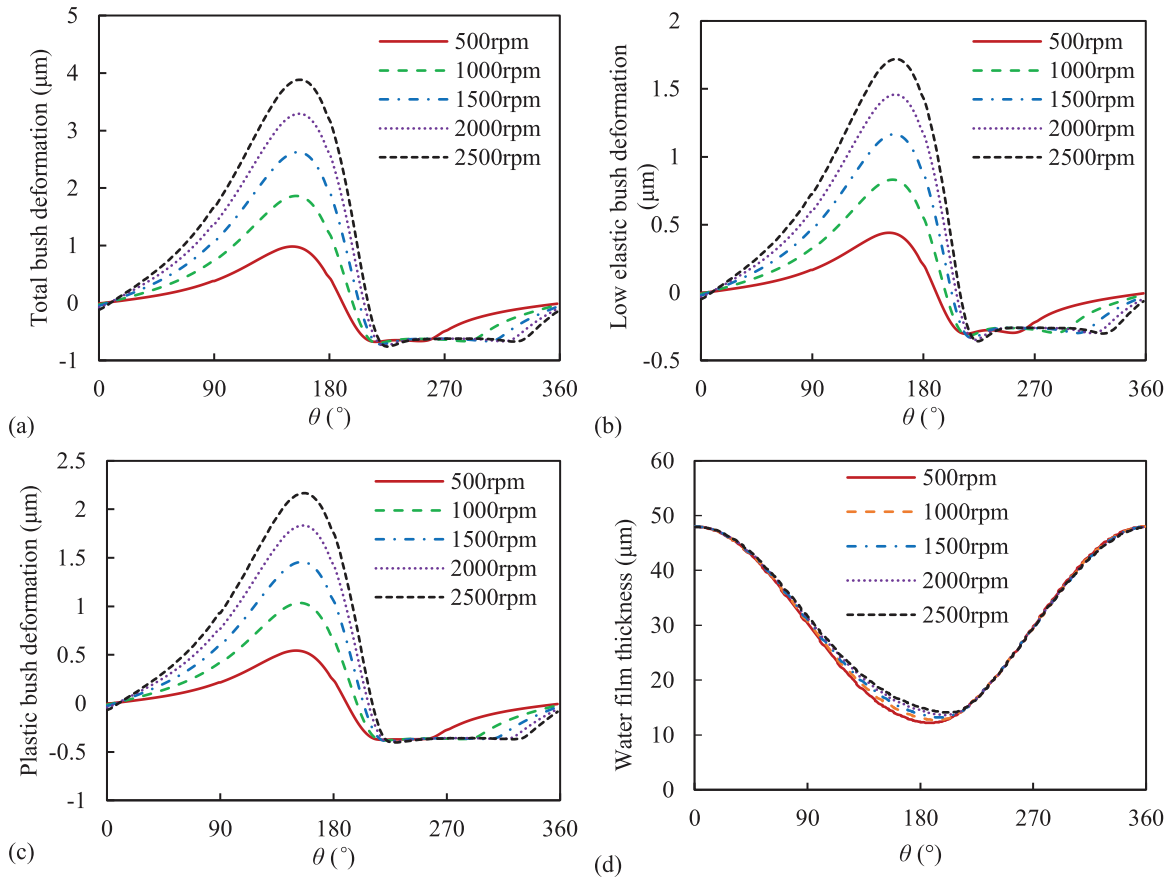

Fig. 10. (a) Bush total deformation distribution, (b) Deformation distribution of low elastic under-layer bush, (c) Deformation distribution of plastic layer bush, (d) Water film thickness distribution for different rotational speed ($\varepsilon = 0.6$, $t_1 = t_2 = 5$ mm, $E_1 = 1000$ MPa, $E_2 = 400$ MPa).

4.4 Effect of bush elastic modulus

Figures 12a–12c shows the radial deformation distribution of double-layer bush, low elastic under-layer bush, and plastic layer bush in the mid-plane of bearing for different low elastic under-layer bush elastic modulus. It can be seen that the bush deformation decreases as the low elastic under-layer bush elastic modulus increases, and the maximum deformation still appears at around $\theta = 153°$. With the increase of the elastic modulus of low elastic under-layer, the deformation curve of low elastic under-layer changes significantly, and the deformation curve of plastic layer bush changes relatively small, which indicates that the change of the total deformation mostly comes from the change of the low elastic under-layer bush deformation. Figure 12d shows the water film thickness distribution for different low elastic under-layer bush elastic modulus. As the low elastic under-layer bush elastic modulus increases from 200 MPa to 1000MPa, the water film thickness in wedge convergence zone decreases, and the maximum reduction is 1.7 μm.

Figures 13a–13e shows the variation of load carrying capacity, attitude angle, maximum water film pressure, friction coefficient and the maximum bearing bush deformation with the low elastic under-layer bush elastic modulus for different eccentricity ratio. Low elastic under-layer bush elastic modulus has a significant impact on the maximum bush deformation especially for large eccentricity ratios, but has little impact on the other lubrication performance parameters. This also indicates that the lubrication performance of double-layer bearing is more similar to that of plastic bearing. For $\varepsilon = 0.6$, as low elastic under-layer bush elastic modulus decreases from 1000 MPa to 200 MPa, the maximum bush deformation increases from 1.8 μm to 3.5 μm, almost doubles. But the load carrying capacity decreases from 854 N to 810 N, only dropping 5.2%. The water film maximum pressure decreases from 0.41 MPa to 0.36 MPa, the attitude angle decreases slowly from 61.5° to 58.2°, and the friction coefficient changes little.

4.5 Effect of bush thickness distribution

Figures 14a–14c shows the radial deformation distribution curves of double-layer bush, low elastic under-layer bush, and plastic layer bush in the mid-plane of bearing for different low elastic under-layer bush thickness. The total bush thickness is 10 mm, as the low elastic under-layer bush thickness increases from 1 mm to 5 mm, the plastic layer bush thickness decreases from 9 mm to

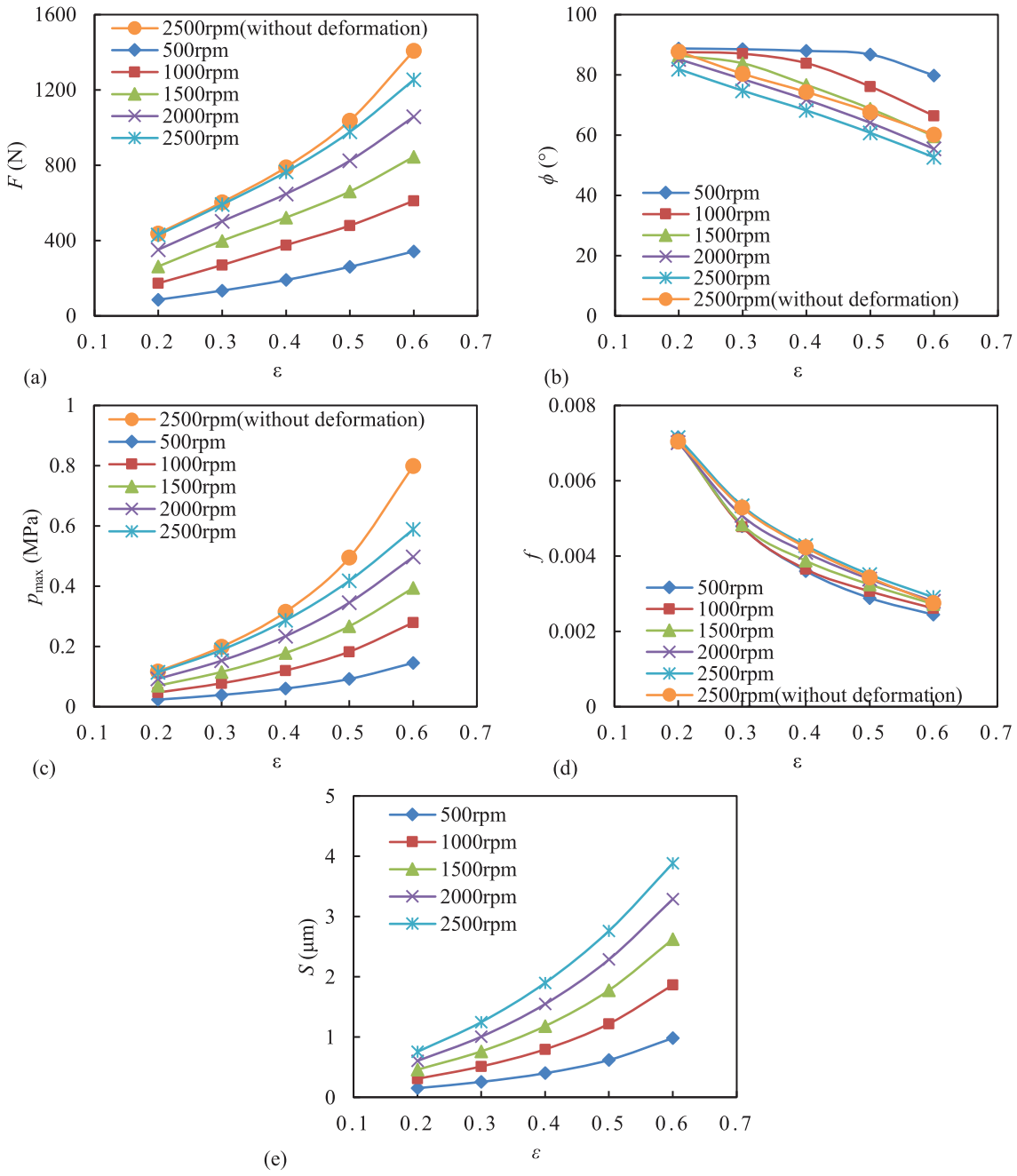

Fig. 11. Effect of rotational speed on the lubrication performance of double-layer bearing (a) Load carrying capacity, (b) Attitude angle, (c) Maximum water film pressure, (d) Friction coefficient, (e) Maximum bearing bush deformation, for t1 = t2= 5 mm, E1 = 1000 MPa, E2 = 400 MPa, n1 = 0.4, n2 = 0.47.

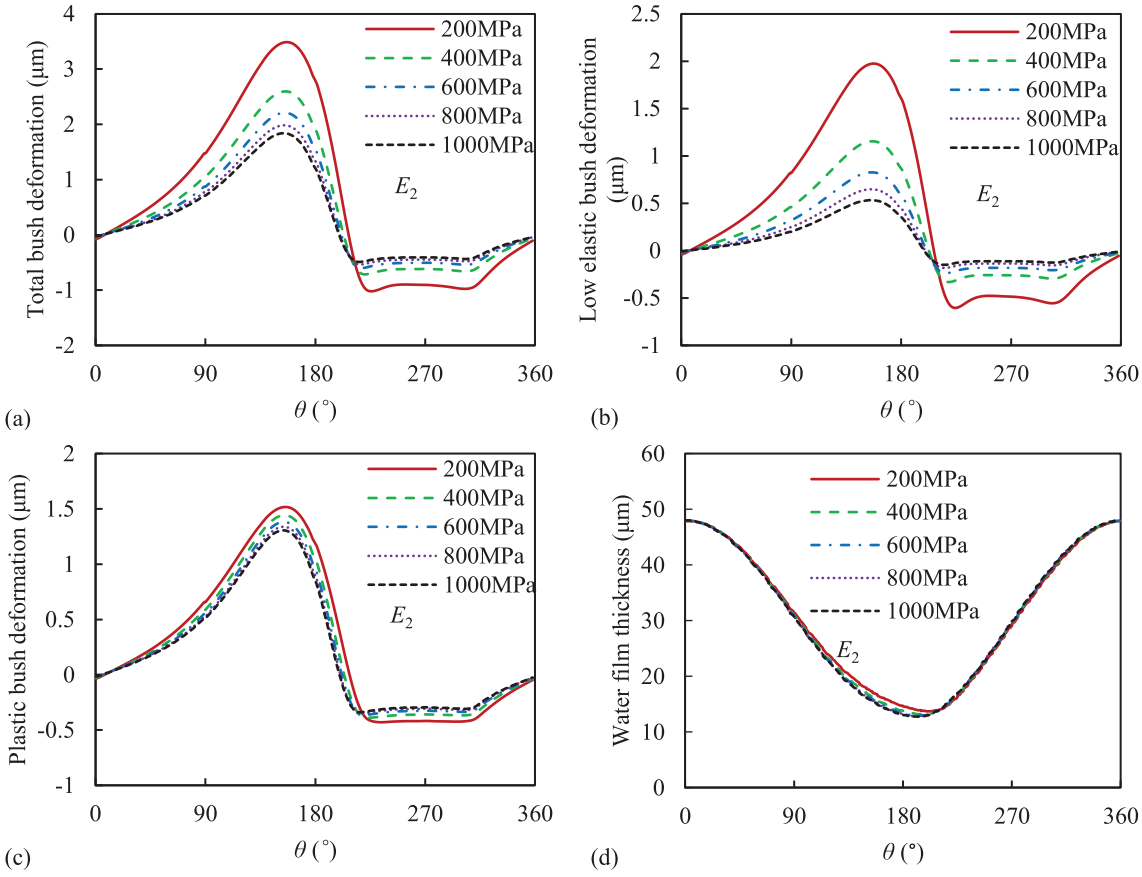

Fig. 12. (a) Bush total deformation distribution, (b) Deformation distribution of low elastic under-layer bush, (c) Deformation distribution of plastic layer bush, (d) Water film thickness distribution for different low elastic under-layer bush elastic modulus ($\varepsilon = 0.6$, $N = 1500$ rpm, $t_1 = t_2 = 5$ mm, $E_1 = 1000$ MPa, $\nu_1 = 0.4$, $\nu_2 = 0.47$).

5 mm. With the increase of low elastic under-layer bush thickness, the deformation of low elastic under-layer bush increases and the deformation of plastic layer bearing bush decreases, but the total bush deformation changes little. Figure 14d shows the water film thickness distribution for different low elastic under-layer bush thickness. It can be seen that the low elastic under-layer bush thickness has little impact on the water film thickness.

Figure 15a–15e shows the variation of load carrying capacity, attitude angle, maximum water film pressure, friction coefficient and the maximum bush deformation with the low elastic under-layer bush thickness for different eccentricity ratio. It can be seen that when the low elastic under-layer bush thickness increases from 1 mm to 5 mm, the lubrication performance parameters change little. For $\varepsilon = 0.6$, the load carrying capacity decreases from 841 N to 836 N, only with a 0.6% drop. The attitude angle decreases from 60.3° to 59.9°, the maximum water film pressure decreases from 0.397 MPa to 0.390 MPa, the maximum bush deformation increases from 2.46 μm to 2.6 μm, and the friction coefficient almost remains the same.

5 Conclusions

This work studies the elastohydrodynamic lubrication performance of double-layer composite water-lubricated bearings using FSI method, and analyzes the influence of rotational speed, eccentricity ratio, low elastic under-layer bush elastic modulus and bush thickness distribution on the lubrication performance of this kind of bearing. The following conclusions are drawn:

– The load carrying capacity of double-layer composite water-lubricated bearing is a little lower than that of plastic bearing and much higher than that of low elastic material bearing. The friction coefficient of double-layer bearing is lower than that of low elastic material bearing and close to plastic bearing. The elastohydrodynamic lubrication performance of double-layer bearing is more like that of plastic bearing.
– Eccentricity ratio and journal rotational speed have significant impacts on the lubrication performance of the bearing. As the eccentricity ratio and journal rotational speed increases, the maximum pressure, the load carrying capacity and the maximum bush deformation increase significantly.

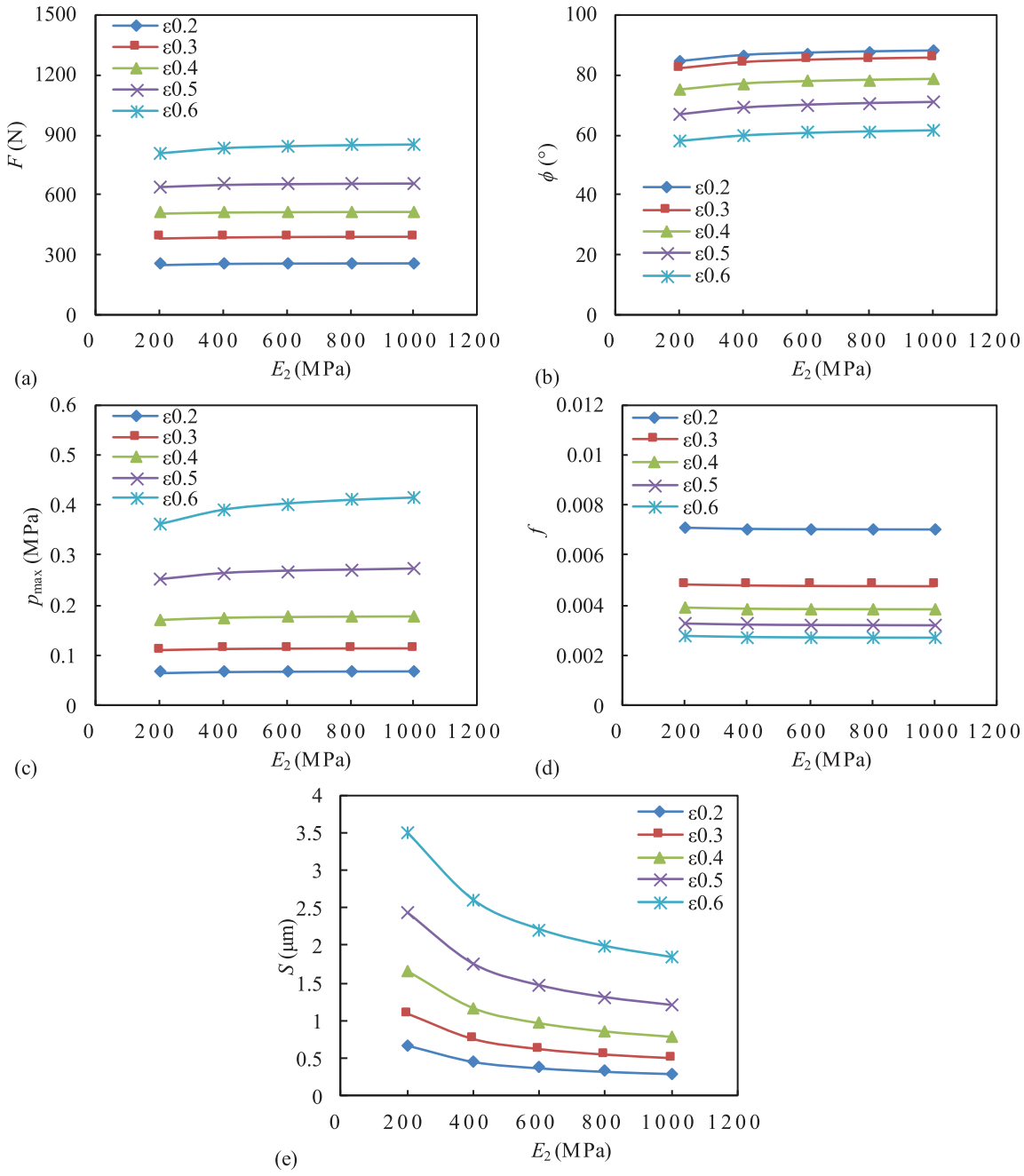

Fig. 13. Effect of low elastic under-layer bush elastic modulus on the lubrication performance of double-layer bearing (a) Load carrying capacity, (b) Attitude angle, (c) Maximum water film pressure, (d) Friction coefficient, (e) Maximum bearing bush deformation, for N = 1500 rpm, t1 = t2 = 5 mm, E1 = 1000 MPa, n1 = 0.4, n2 = 0.47.

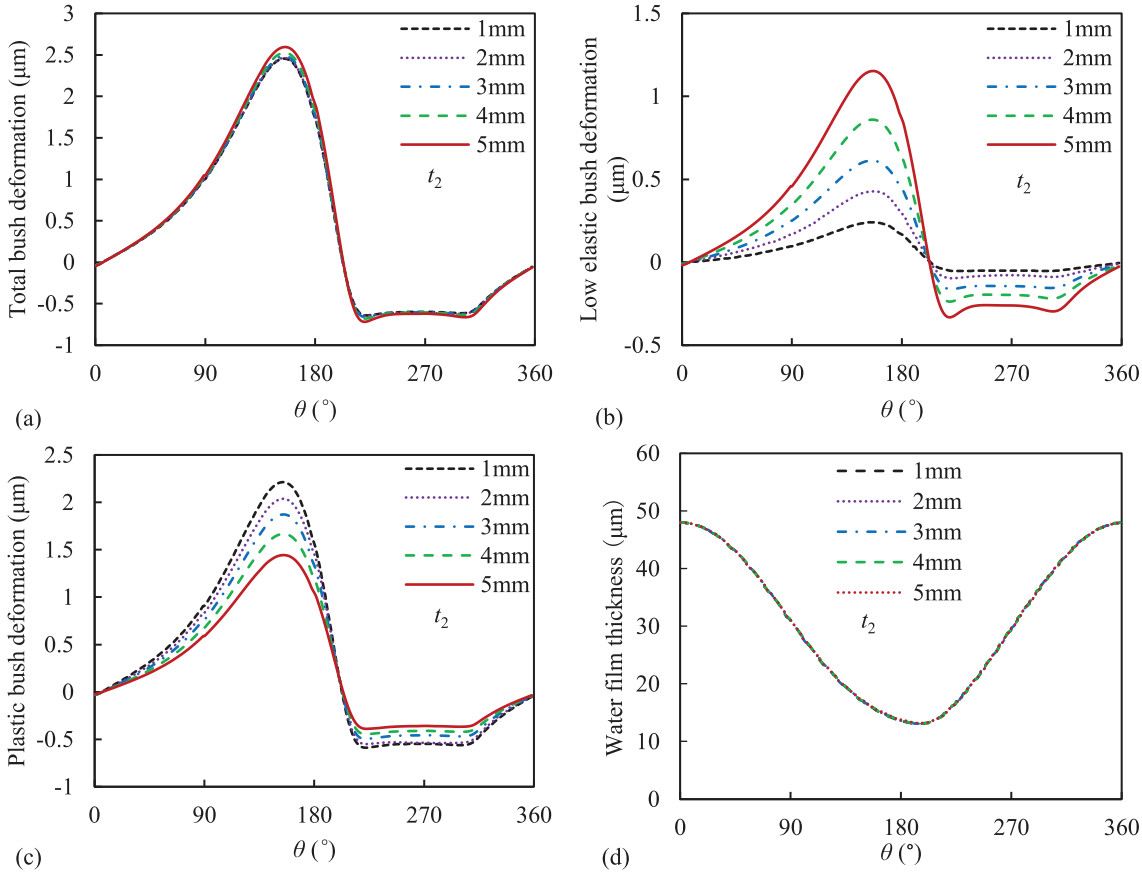

Fig. 14. (a) Bush total deformation distribution, (b) Deformation distribution of low elastic under-layer bush, (c) Deformation distribution of plastic layer bush, (d) Water film thickness distribution for different low elastic under-layer bush thickness ($\varepsilon = 0.6$, $N = 1500$ rpm, $E_1 = 1000$ MPa, $E_2 = 400$ MPa, $\nu_1 = 0.4$, $\nu_2 = 0.47$).

– Low elastic under-layer bush elastic modulus has a significant impact on the maximum bush deformation especially for large eccentricity ratios, but has little impact on the other lubrication performance. For $\varepsilon = 0.6$, as low elastic under-layer bush elastic modulus decreases from 1000 MPa to 200 MPa, the maximum bush deformation almost doubles, but the load carrying capacity drops only 5.2%. The change of the total deformation mainly comes from the low elastic under-layer bush deformation, which indicates that the double-layer bearing has better load carrying capacity than low elastic material bearing.
– Bush thickness distribution influences the deformation of both low elastic under-layer bush and plastic bush, but have little impact on the total bush deformation. The load carrying capacity, the attitude angle, the maximum water film pressure and the friction coefficient change little as the low elastic under-layer bush thickness increases from 1 mm to 5 mm.

Nomenclature

c	Radial clearance
e	Eccentricity of journal
f	Friction coefficient
F	Load carrying capacity
L	Bearing length
$p_{\max}$	Maximum water film pressure
t_1	Thickness of plastic bush
ν_1	Poisson's ratio of plastic bush
ε	Eccentricity ratio $= e/c$
ϕ	Attitude angle
O_b	Bearing center
D	Bearing inner diameter
E_1	Elastic modulus of plastic bush
E_2	Elastic modulus of low elastic under-layer bush
$h_{\min}$	Minimum film thickness
N	Rotational speed of journal
S	Maximum deformation of bearing bush
t_2	Thickness of low elastic under-layer bush
ν_2	Poisson's ratio of low elastic under-layer bush
μ	Viscosity of lubricant
θ	Bearing angle, or angular coordinate
O_j	Journal center

Funding Information

The financial supports from National Natural Science Foundation of China (Grant No. 51905317) and Shandong Provincial Key Laboratory of Precision Manufacturing and Non-traditional Machining are gratefully acknowledged.

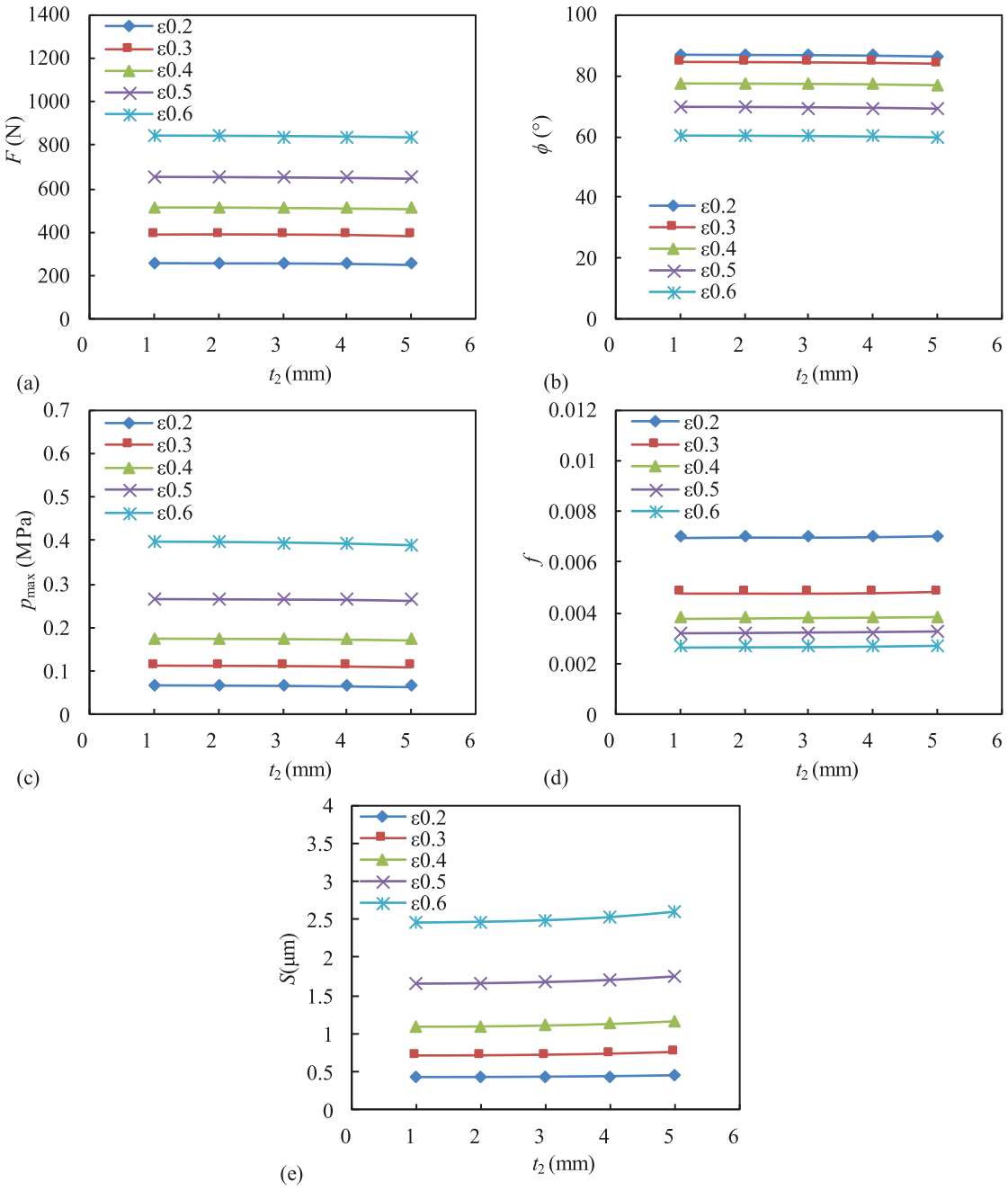

Fig. 15. Effect of low elastic under-layer bush thickness on the lubrication performance of double-layer bearing (a) Load carrying capacity, (b) Attitude angle, (c) Maximum water film pressure, (d) Friction coefficient, (e) Maximum bearing bush deformation, for N = 1500 rpm, E1 = 1000 MPa, E2 = 400 MPa, n1 = 0.4, n2 = 0.47.

References

[1] W. Litwin, Water-lubricated bearings of ship propeller shafts – problems, experimental tests and theoretical investigations, Pol. Maritime Res. **16**, 41–49 (2009)

[2] H. Wang, Z. Liu, L. Zou et al., Influence of both friction and wear on the vibration of marine water lubricated rubber bearing, Wear **376–377**, 920–930 (2017)

[3] E. Piątkowska, Influence of solid particle contamination on the wear process in water lubricated marine strut bearings with NBR and PTFE bushes, Pol. Maritime Res. **28**, 167–178 (2022)

[4] Z. Yan, X. Zhou, H. Qin et al., Study on tribological and vibration performance of a new UHMWPE/graphite/NBR water lubricated bearing material, Wear **332–333**, 872–878 (2015)

[5] A.B. Ali, M.A. Samad, N. Merah, UHMWPE hybrid nanocomposites for improved tribological performance under dry and water-lubricated sliding conditions, Tribol. Lett. **65**, 102 (2017)

[6] Z. Yang, Z. Guo, Z. Yang et al., Study on tribological properties of a novel composite by filling microcapsules into UHMWPE matrix for water lubrication, Tribol. Int. **153**, 106629 (2021)

[7] Duramax Marine, https://www.duramaxmarine.com/advanced-bearings/romor-i-dovetail-stave-bearings.htm (accessed 17 February 2022)

[8] M. Wodtke, W. Litwin, Water-lubricated stern tube bearing – experimental and theoretical investigations of thermal effects, Tribol. Int. **153**, 106608 (2021)
[9] W. Litwin, Properties comparison of rubber and three layer PTFE-NBR-bronze water lubricated bearings with lubricating grooves along entire bush circumference based on experimental tests, Tribol. Int. **90**, 404–411 (2015)
[10] W. Litwin, Experimental research on water lubricated three layer sliding bearing with lubrication grooves in the upper part of the bush and its comparison with a rubber bearing, Tribol. Int. **82**, 153–161 (2015)
[11] D. Cabrera, N. Woolley, D. Allanson et al., Film pressure distribution in water-lubricated rubber journal bearings, Proc. Inst. Mech. Eng. J **219**, 125–132 (2005)
[12] A. Kraker, R. Ostayen, D. Rixen, Calculation of Stribeck curves for (water) lubricated journal bearings, Tribol. Int. **40**, 459–469 (2007)
[13] Y. Liao, Y. Zhou, Analysis on the lubrication characteristics of a few aqueous media that affect water lubricated rubber alloy bearing, J. Mech. Sci. Technol. **31**, 4771–4779 (2017)
[14] Y. Wang, Z. Yin, D. Jiang, G. Gao, X. Zhang, Study of the lubrication performance of water-lubricated journal bearings with CFD and FSI method, Ind. Lubric. Tribol. **68**, 341–348 (2016)
[15] X.S. Lao, C.H. Dai, Y. Liu et al., Performance study on modified UHMWPE composites water lubricated bearing material, Mater. Sci. Forum **947**, 167–172 (2019)
[16] G. Zhou, J. Wang, Y. Han et al., An experimental study on film pressure circumferential distribution of water-lubricated rubber bearings with multiple grooves, Tribol. Trans. **60**, 385–391 (2017)
[17] G. Zhou, X. Mi, J. Wang et al., Experimental comparison between the Stribeck curves of water lubricated rubber bearing with straight and spiral grooves, Ind. Lubric. Tribol. **70**, 1326–1330 (2018)
[18] Z. Zhao, Z. Rui, Theoretical and experimental analysis of a water-lubricated rubber journal bearing with a large aspect ratio, Ind. Lubric. Tribol. **72**, 797–803 (2020)
[19] Y. Wang, X. Shi, L. Zhang, Experimental and numerical study on water-lubricated rubber bearings, Ind. Lubric. Tribol. **66**, 282–288 (2019)
[20] L. Huang, Y. Jin, Z. Liu, L. Zou, The effect of damping layer on the dynamic performance of water-lubricated rubber bearings, Noise Vibr. Control **36**, 32–37 (2016)
[21] J.L. Cai, G. Xiang, S. Li, Mathematical modeling for nonlinear dynamic mixed friction behaviors of novel coupled bearing lubricated with low viscosity fluid, Phys. Fluids **34** (2022)
[22] ANSYS, ANSYS F FLUENT, version 14.0: user manual (ANSYS Inc., Canonsburg, USA, 2011)
[23] P.J. Zwart, A.G. Gerber, T. Belamri, A two-phase flow model for predicting cavitation dynamics, in Proceedings of the fifth international conference on multiphase flow, Yokohama, Japan (2004)

Cite this article as: Z. Yang, X. Zhang, Y. Wang, Y. Zhao, Study on elastohydrodynamic lubrication performance of double-layer composite water-lubricated bearings, Mechanics & Industry **24**, 3 (2023)